Earthquake stability calculation of basein for aquacultur in acordance with rules of Eurocode 8

Final report

In accordance with the contract B-21770N-085

Project coordinator: Dr.Phys. Andris Jakovics

Responsible executor: Master of Science in Engineering Jevgēņijs Teličko

Riga, February 2025

Contents

1. Introduction

The report presents the results of a numerical analysis in the context of contract B-21770N-085 with AmfiTop Aqua Forming LTD in accordance with the procedures of Eurocode 8 and defined work plan APPENDIX A.

In this report, Section 2 examines various engineering approaches that are most suitable for analyzing the studied structure.

In Section 3, the suitability of the construction is evaluated in accordance with Eurocode 8. For this purpose, several numerical models developed using COMSOL Multiphysics and Elmer OpenFOAM are employed. Subsequently, the construction evaluation process and the parameters used are described.

Then, Section 4 presents the mesh evaluation process and the optimized geometry design.

Finally, conclusions are provided in section 5.

2. A detailed analysis of existing research on approaches to evaluate constructions in seismic action

The evaluation of structures under seismic conditions can be a complex numerical task. When modeling the full geometry and comprehensively accounting for all physical processes (e.g., the movement and interaction of liquid with a solid body), even high-performance computers may lack the necessary resources. However, for analyzing structures under seismic conditions, many established engineering codes are available that simplify the numerical problem. According to widely adopted practices, these methods can be categorized into four types [1, 2]:

- Lateral Force Method (LFM) and Modal Response Spectrum Analysis (MRSA), which assume linear structural behavior.
- Non-Linear Static Analysis (NLSA), also known as Pushover Analysis, and Non-Linear Time-History Analysis (NLTHA), which consider nonlinear structural behavior.

In general, linear methods demand fewer computational resources; however, not all engineering codes can guarantee safe results under such simplifications [3, 4]. Despite this, linear models are more commonly employed for building simulations due to their reduced computational requirements.

When modeling liquid-containing vessels, studies often employ engineering codes such as API 650, AWWAD-100, Eurocode 8 Part 4, and ACI 350.3-06, among others [5, 6, 7, 8]. These codes generally assume a linear approach, where the analysis presumes a proportional relationship between loads and responses, simplifying the calculations.

It is important to note, however, that although all these codes are designed for evaluating liquid-containing vessels, their areas of application differ.

ACI 350.3-06 is focused on evaluating concrete structures. In contrast, API 650 and AWWAD-100 are more oriented toward assessing welded metallic tanks. Eurocode 8 Part 4, compared to the aforementioned codes, appears to be a more universal solution as it facilitates the evaluation of various types of structures, such as silos, pipes, and tanks made from different materials[1]. It is also critical to emphasize that an engineering code does not directly evaluate a structure. Instead, it provides simplified boundary conditions that significantly reduce the complexity of calculations involving physical processes such as fluid motion and its interaction with solid bodies.

For the numerical evaluation of structures using simplified boundary conditions, software such as ANSYS, Comsol Multiphysics, and SAP2000 is frequently employed [8, 9]. Some programs, such as Comsol Multiphysics, even feature built-in modules for spectral analysis of structural designs.

3. Description of the methodology for simplifying dynamic calculations based on studies and their results reported in the literature

Based on the analysis of modeling examples for similar structures, it is evident that solving such a problem with full-scale modeling without simplifications is not feasible. It can also be noted that even when employing simplified methods, the authors of the reviewed studies apply additional simplifications to the structure. Specifically, they model the tank walls as shells with equivalent properties, which significantly reduces the number of elements.

3.1. Approximation of construction with cilinder

To simplify the assessment of the structure under seismic loading, Eurocode 8 Part 4 could potentially be utilized. However, it is important to mention that this engineering code, first and foremost, assumes the use of a cylindrical structure. In contrast, as shown in Figure 3.1, the geometry provided by the client features an angular shape.

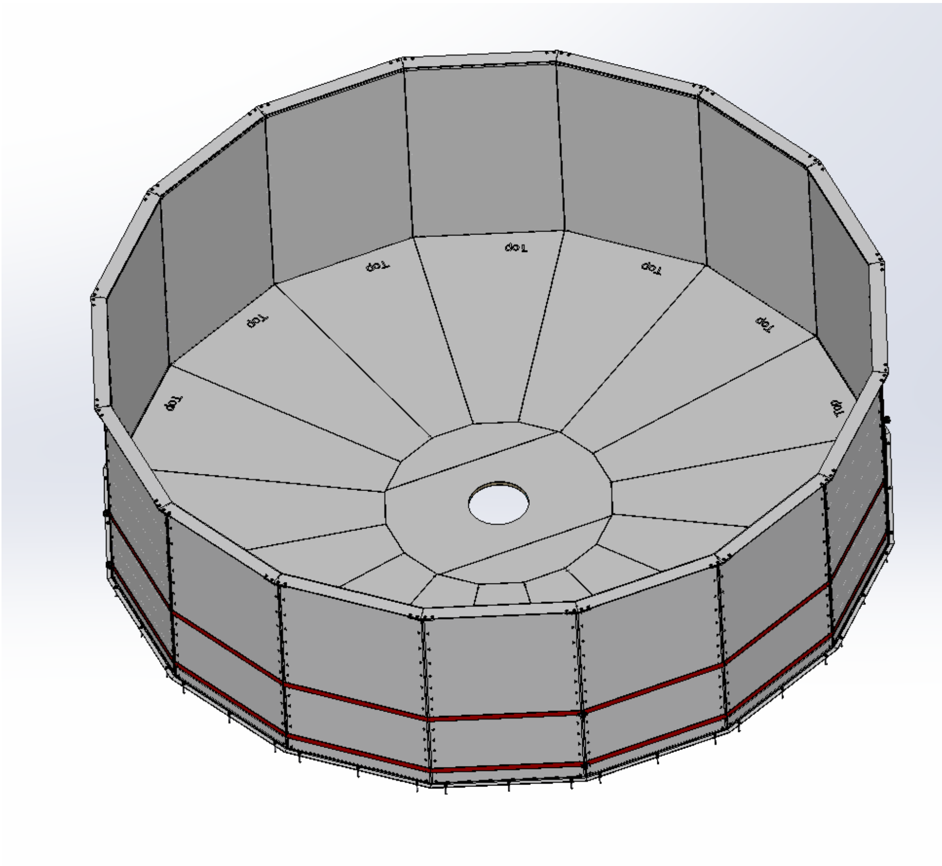

Fig. 3.1. *Original cunstruction design with 16 wall elements*

It is important to note that the simplification of calculations using Eurocode 8 lies in determining the pressure exerted by the liquid without modeling the liquid itself. Since overlaying a circle on the structure (see Fig. 3.2) shows that the geometry of the tested structure is relatively close to a cylindrical shape, this approach may be feasible.

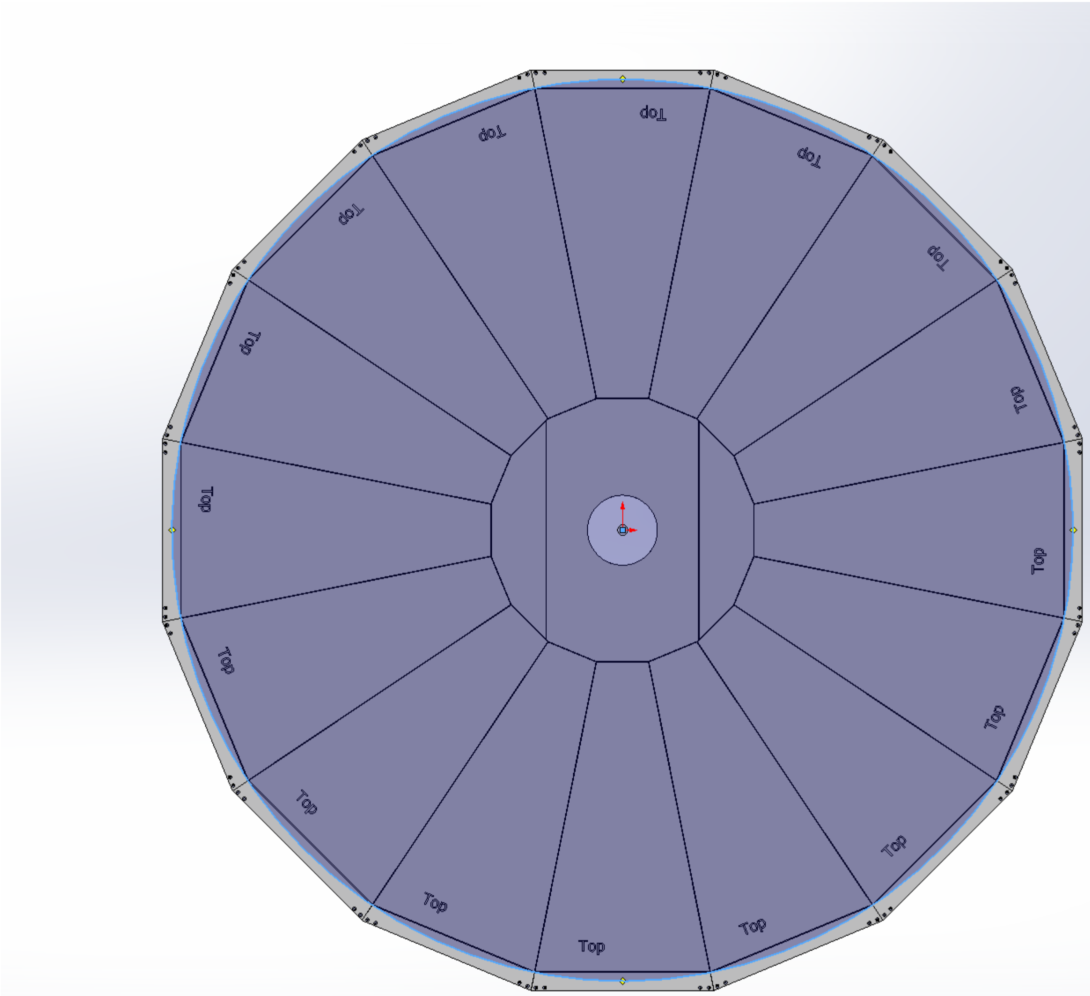

Fig. 3.2. *Original cunstruction design with 16 wall elements view from top*

To numerically evaluate the similarity of the geometry and the potential differences in pressures caused by fluid motion, a simplified numerical model can be employed. This model accounts for fluid pressure resulting from lateral acceleration of the structure but does not consider the deformation of the solid body.

For constructing the simplified cylindrical geometry, the radius shown in Fig. 3.2 was used as a basis. Consequently, the volume of fluid in the cylinder is 2% greater than that in the original structure. To perform the numerical comparison, Comsol Multiphysics was utilized. For modeling fluid motion and the phase interface, the Two-Phase Flow, Phase Field, and Laminar Flow modules were applied. Both models used the same mesh size, resulting in 61,000 elements for the cylindrical geometry and 67,000 elements for the hexadecagonal geometry.

The applied acceleration was the maximum recorded acceleration in Norway (0.581 m/s^2) over a 2-second duration. The results of the calculations are shown in Fig. 3.3.

As seen in the figure, the pressure distribution and its minimum values are identical. In contrast, the maximum values differ, with the cylindrical geometry showing a 1.3% higher pressure, likely due to the slightly larger volume of water or differences in the meshes.

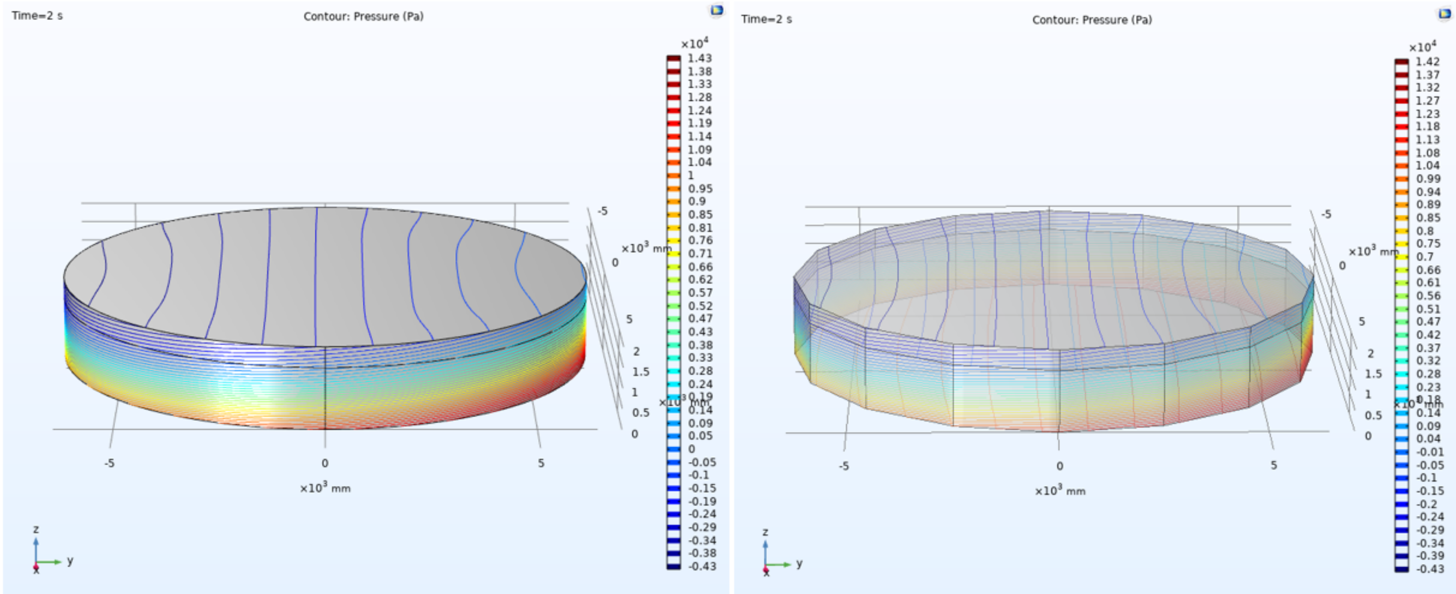

Fig. 3.3. *Pressure distribution in hexadecagon and cylindrical equivalent.*

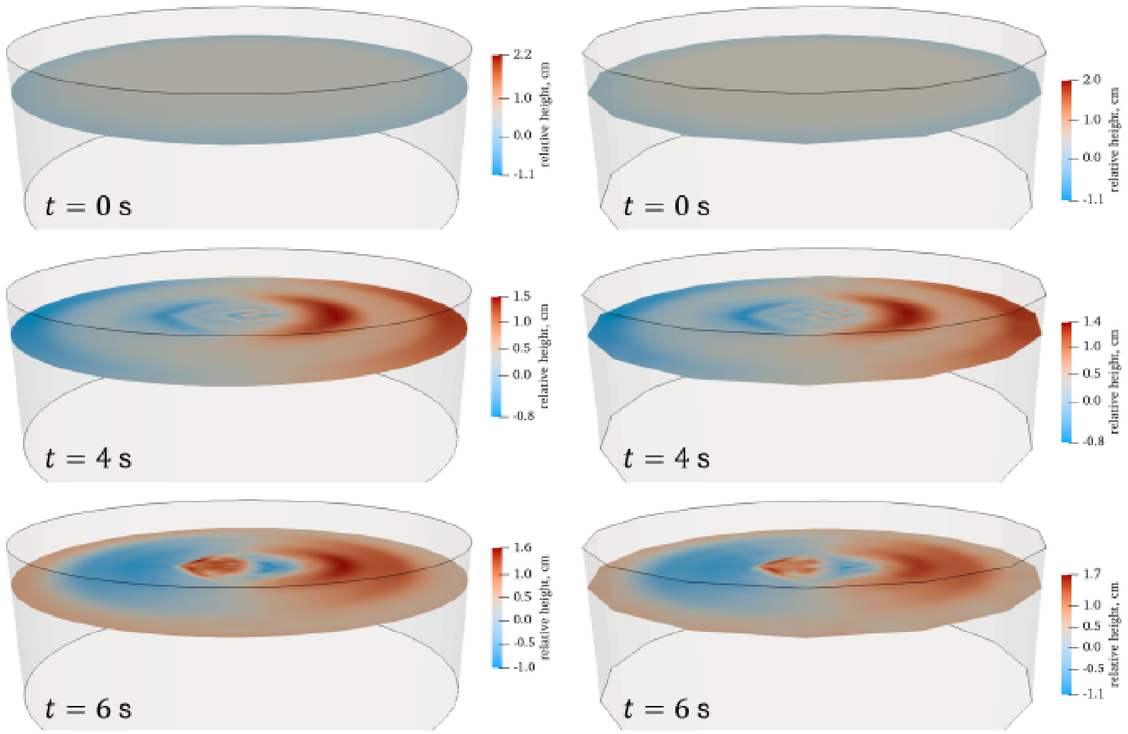

Fig. 3.4. *OpenFOAM results*

The second equivalence of the pool shape to a cylinder is presented as follows. Two hydrodynamic numerical simulations are performed—one for a cylinder and the other for the rectangular shape considered in this study. The numerical analysis is conducted using OpenFOAM v8, employing the two-phase solver interFoam. The model consists of same geometry as before. A horizontal acceleration, depicted on the right side of fig. 3.8 , is applied to the pool using the built-in tabulated AccelerationSource function in OpenFOAM, which allows specifying the acceleration in the form of a timetable. The simulation is performed up to t=10 s.

Both pool shapes can be considered equivalent (in a purely hydrodynamic context) if the resulting free surface waves in both cases are very similar, including their characteristic wave amplitudes and frequencies. Figure 3.4 illustrates the free surface shapes and heights relative to the initial state. Under the given horizontal acceleration, the relative surface height in both cases does not exceed 4 cm.

It is also worth noting that Eurocode 8 Part 4 is not explicitly intended for the evaluation of aluminum structures. The code provides guidelines primarily for analyzing concrete structures. In such cases, the load generated by the liquid is divided into two components: pressure representing convection and pressure representing the fluid's impulse. The code emphasizes the importance of considering the mass of the tank walls in this case.

Analyzing the surface waves over time revealed that both geometries are practically identical. The straight segments along the perimeter of the rectangular pool only cause minor perturbations in the free surface. Large-scale wave motion is almost identical to that observed in the circular pool. This implies that, in a hydrodynamic context, the rectangular pool can be considered equivalent to a circular one. Consequently, the pressure expressions defined in Eurocode 8 can be applied to the pool under investigation in this study.

For the analysis of steel structures, the code indicates that the mass of the walls can be neglected; however, it is essential to account for the pressure generated during wall deformation. In the case of the tested geometry, since aluminum has a lower density than steel, the impulse of the structure itself is unlikely to significantly affect the stress. However, the structure is not thin-walled and gains stiffness from aluminum profiles inside the wall see fig 3.5.

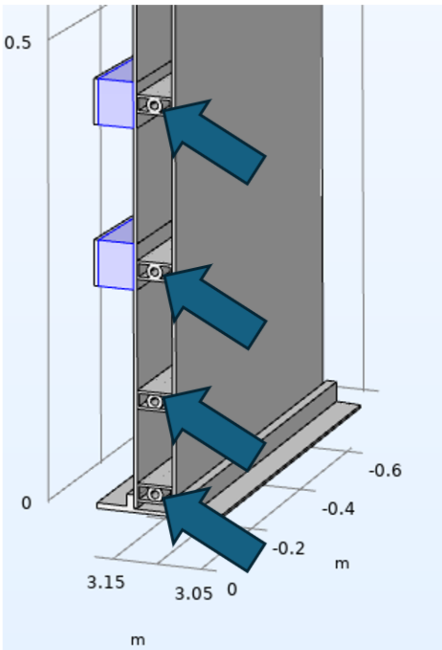

Fig. 3.5. *Pool single wall construction and inner profile alocation*

To identify the most suitable analysis method iteratively, it is important to evaluate the acceleration of wall deformation, as this plays a critical role in the pressure associated with wall deformation. For this purpose, the pressure equations for concrete structures may be applied: see equation 1 and 2 from Eurocode 8 part 4 [1].

$$p_i(\xi, \zeta, \theta, t) = C_i(\xi, \zeta)\rho H \cos(\theta) A_g(t) \tag{3.1}$$

$$p_c(\xi, \zeta, \theta, t) = \rho \textstyle\sum_{n=1}^{\infty} \psi_n \cosh(\lambda_n \gamma(\zeta)) J_1(\lambda_n \xi) \cos(\theta) A_{cn}(t) \tag{3.2}$$

$$p_v(\zeta, t) = \rho H(1-\zeta) A_v(t) \tag{3.3}$$

Where $p_i(\xi, \zeta, \theta, t)$ represent impulsive pressure, $p_c(\xi, \zeta, \theta, t)$ represent convective pressure and $p_v(\zeta, t)$ represent vertical pressure caused by vertical acceleration. $\xi = r/R$, $\zeta = z/H$, R - tank radius, H - liquid height, ρ - liquid density , $A_g(T)$ - acceleration over time (generated from the spectrum in this study), $I_i(x)$ - modified Bessel function of the first kind with order i, $I'_1(x) = I_0(x) - \frac{I_1(x)}{x}$, $\nu_n = \pi\frac{2n+1}{2}$, $\gamma = \frac{H}{R}$, $J_i(x)$ - Bessel function of the first kind with order i,

$\lambda_1 = 1.841$, $\lambda_2 = 5.331$, $\lambda_3 = 8.536$, $A_{cn}(t)$ - acceleration over time for a single-degree-of-freedom oscillator with angular acceleration,

$$\omega_{cn} = \sqrt{\frac{g\lambda_n}{R} tanh(\lambda_n \gamma)}$$

g - gravitational acceleration. Eurocode 8 specifies that for the calculation of p_c, it is sufficient to consider only the first oscillatory mode ($n = 1$), $A_v(t)$ is the time dependence of the vertical acceleration (generated from the spectrum in this study).

3.2. Seismic Action

Earthquakes can be characterized by ground acceleration in the horizontal and vertical directions. This acceleration is typically described by an acceleration spectrum, which shows the oscillations of the Earth at different frequencies (periods). Such spectra are usually obtained from ground acceleration measurements during an earthquake. Fig. 3.6 presents an example of a real earthquake spectrum and its corresponding time signal.

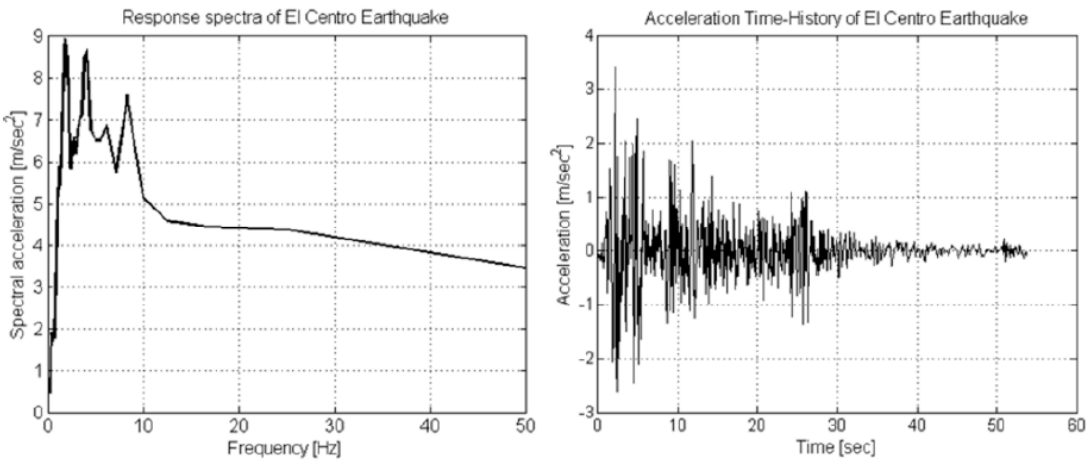

Fig. 3.6. *The Earth's acceleration spectrum and the corresponding time signal. Image from [10]*

The analysis of structural stability is usually performed based on the characteristic earthquake parameters of the specific building's location. eurocode 8 defines the shape of the earthquake spectrum curve, which depends on various parameters, such as soil type, maximum ground acceleration, etc. For horizontal ground acceleration, the spectrum is given in equesion 3.4:

$$S_e(T) = \begin{cases} a_g S\left[1 + \frac{T}{T_B}(2.5\eta - 1)\right], & 0 \le T \le T_B \\ 2.5 a_g S\eta, & T_B \le T \le T_C \\ 2.5 a_g S\eta\left[\frac{T_C}{T}\right], & T_C \le T \le T_D \\ 2.5 a_g S\eta\left[\frac{T_C T_D}{T^2}\right], & T_D \le T \le 4s \end{cases} \tag{3.4}$$

where $S_e(T)$ is the elastic ground oscillation spectrum, T is the oscillation period, a_g is the acceleration for Type A ground (solid rock), T_B, T_C, T_D are characteristic periods of different types of oscillations, S is the soil factor, and η is the damping correction factor (for 5% viscous damping, $\eta = 1$).

For vertical acceleration, the expressions are very similar to those for horizontal acceleration.

$$S_{ve}(T) = \begin{cases} a_{vg}\left[1 + \frac{T}{T_B}(3\eta - 1)\right], & 0 \le T \le T_B \\ 3a_{vg}\eta, & T_B \le T \le T_C \\ 3a_{vg}\eta\left[\frac{T_C}{T}\right], & T_C \le T \le T_D \\ 3a_{vg}\eta\left[\frac{T_C T_D}{T^2}\right], & T_D \le T \le 4s \end{cases} \tag{3.5}$$

In this work, the following parameter values provided by the customer see APPENDIX B are used:

$S_e(T)$	a_g, m/s^2	S	T_B, s	T_C, s	T_D, s
	0.5832	1	0.05	0.25	1.2

$S_{ve}(T)$	a_{vg}, m/s^2	T_B, s	T_C, s	T_D, s
	$0.45a_g$	0.05	0.15	1.0

With the given values, the following spectra are defined (see Fig.) 3.7:

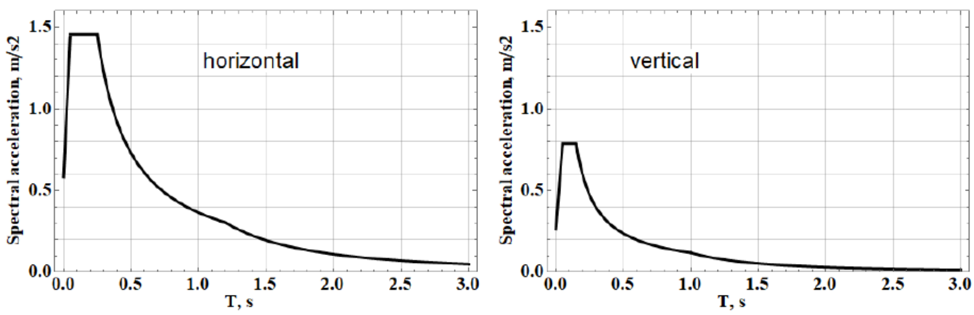

Fig. 3.7. *Horizontal (on the left) and vertical (on the right) acceleration spectrum*

If the impact of an earthquake on the structure of a construction is modeled numerically in a time-dependent manner, then the acceleration spectrum cannot be directly applied – a real-time signal must be used. eurocode 8 defines only the spectrum, without providing the corresponding time signal. There are basically two options – to use a recorded acceleration signal from a real earthquake, or to generate an artificial acceleration time signal based on the spectrum defined by Eurocode 8. In this work, the second approach is used.

Generating an artificial signal is generally not a simple task, as the spectrum does not contain phase information of the oscillations. There are various commercial programs that generate such data. In this work, the Matlab code provided in [11] is used. This approach is based on adapting real earthquake acceleration data to the user-defined spectrum. As a result of data adaptation, a realistic ground acceleration time history is obtained, which corresponds to the spectrum defined according to the Eurocode 8 methodology. Fig. 3.8 shows the spectrum and the generated time dependence.

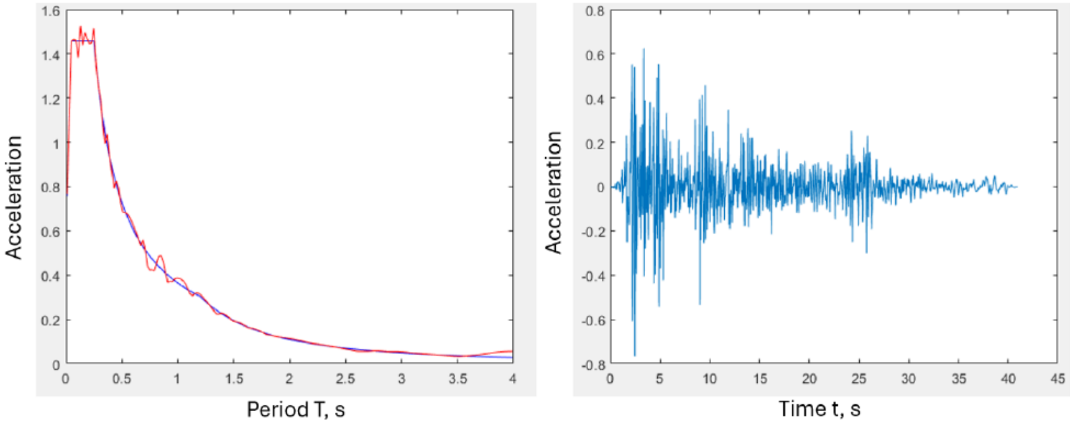

Fig. 3.8. *Horizontal acceleration spectr (on the left) and Horizontal (on the right) acceleration*

3.3. Geometry, Material Properties and loads

The following material properties were used for the evaluation of this structure:

For the aluminum components, the properties of AA6060-T4 were applied (see Table 3.1). For components made of 'solid surface' material, their properties can be found in Table 3.2. Additionally, for the metallic strip, the properties from Table 3.3 were used.

Table 3.1. *Solid surface Properties*

Young's modulus	68.2 (GPa)
Poisson's ratio	0.33
Density	2800 (kg/m^3)

Table 3.2. *Solid surface Properties*

Young's modulus	4.79(GPa)
Poisson's ratio	0.3
Density	1020 (kg/m^3)

Table 3.3. *s355 Properties*

Young's modulus	200 (GPa)
Poisson's ratio	0.3
Density	7850 (kg/m^3)

3.4. Verification of small deformations

To evaluate deformations and the impact of pressure caused by the structural deformation, a numerical model of a single wall was developed using symmetry. The considered symmetry segment is shown in Figure 3.9. In Figure 3.9, the blue lines represent the symmetry planes, while the blue arrow indicates the analyzed segment.

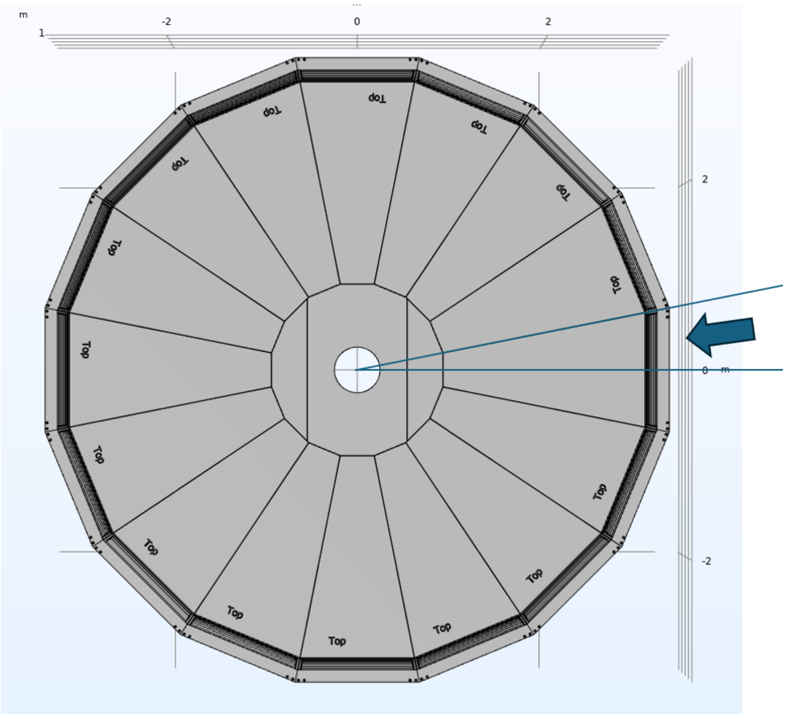

Fig. 3.9. *Symmetry planes*

It is important to note that the pressures provided by the Eurocode 8 depend on geometric characteristics such as the tanks's radius and the water height. Additionally, in the equation for the impulsive component, the presence of the cosine function causes the pressure to vary along the circumference, reaching its maximum at an angle of 0 degrees.

In this case, the numerical model was used to analyze a tank with a water level of 1.75 meters and a radius of 6 meters. The wall segment was positioned in such a way that the sum of the convective and impulsive pressures was maximized at the center of the wall.

Thus, for this calculation, the total applied pressure included the sum of hydrostatic water pressure, convective water pressure, and impulsive water pressure , and pressure caused by vertical acceleration. This represents a more conservative approach, as it ensures that the maximum pressure is considered for every wall segment of the structure.

To simplify the model, small elements such as bolts and nuts were excluded.

Additionally, to further simplify the model, the upper fastening element and the sheet made of solid surface material on the inner side of the basin were removed. This, in turn, makes the created model slightly more conservative, as these elements could contribute to the overall structural rigidity.

In the numerical model, the connections between the stiffening profiles and the aluminum plates of the wall segments were represented as infinitesimally small springs. The compressive stiffness of these springs was set equal to the yield strength of the stressed materials, while the tangential stiffness was set to zero.

As a result, when the wall segment deforms, the structural ribs will experience greater deformation since the wall plate and the profile are not considered as a single integral component and are allowed to slide relative to each other.

The location of this boundary condition is shown in blue in Figure 3.10.

In Fig. 3.11, the maximum deformation of the structure in time can be observed.

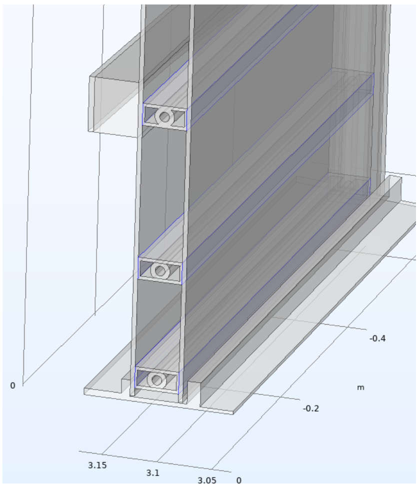

Fig. 3.10. *Sliding boundary of profiles and pool walls*

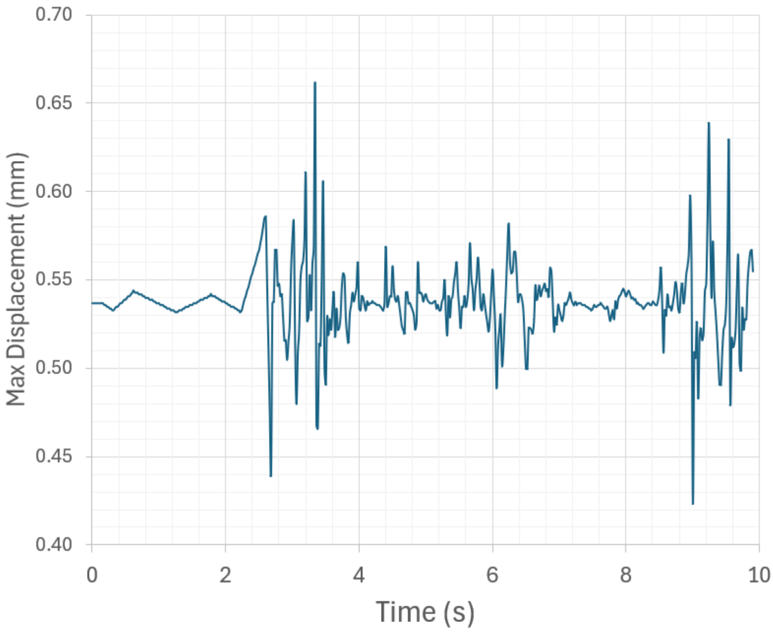

Fig. 3.11. *Max displacement in time*

As can be seen, the deformation caused by this load does not exceed one millimeter and is primarily due to the static load, which initially deforms the structure by 0.54 mm. The maximum deformation was reached at 3.34 seconds of the simulation, at the peak of seismic activity, and amounted to 0.64 mm. The distribution of deformations on the wall segment can be observed in Figure 3.12.

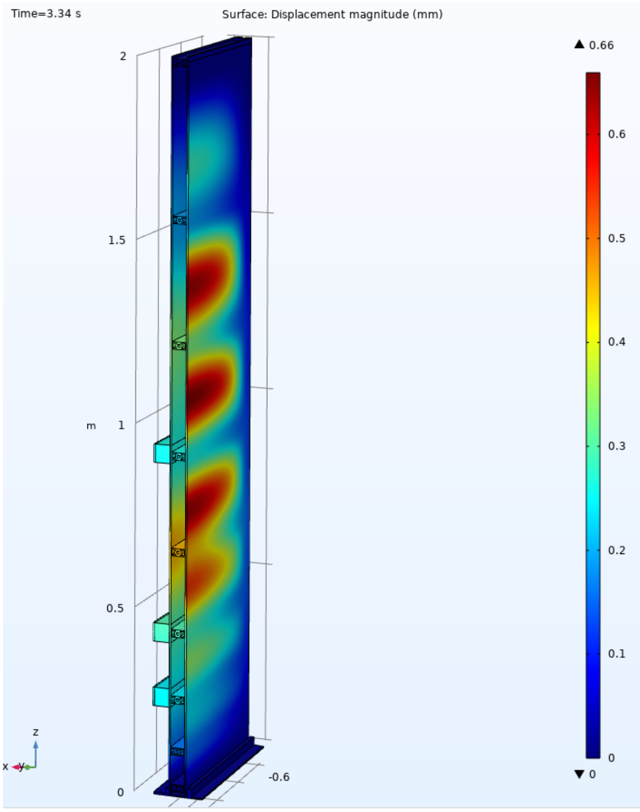

Fig. 3.12. *Wall displacement at 3.34 second*

In Figure 3.13, the graph of the maximum stress in the structure over time is shown. From this, it can be concluded that the yield limits for aluminum and steel (60MPa, 200MPa) were not exceeded, as the maximum stress value remained within the allowable limits.

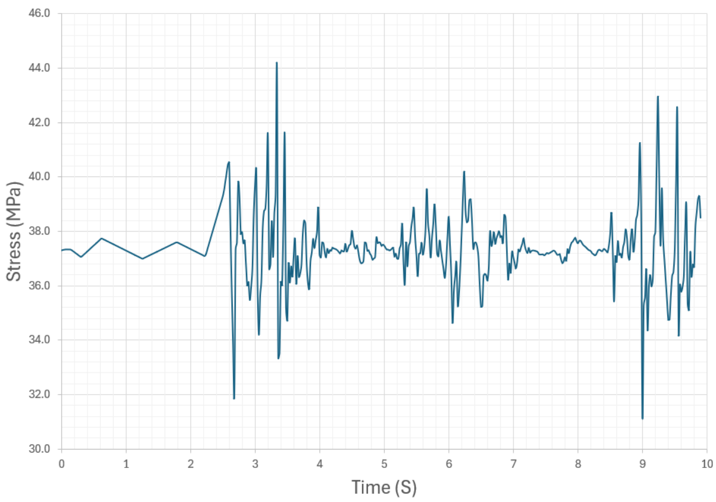

Fig. 3.13. *Max stress in time*

In turn, Figure 3.14 presents the stress graph for the spacers between the wall and the steel straps made of Solid Surface material. From this graph, it can be observed that the yield limit (15 MPa) of the Solid Surface material was also not exceeded.

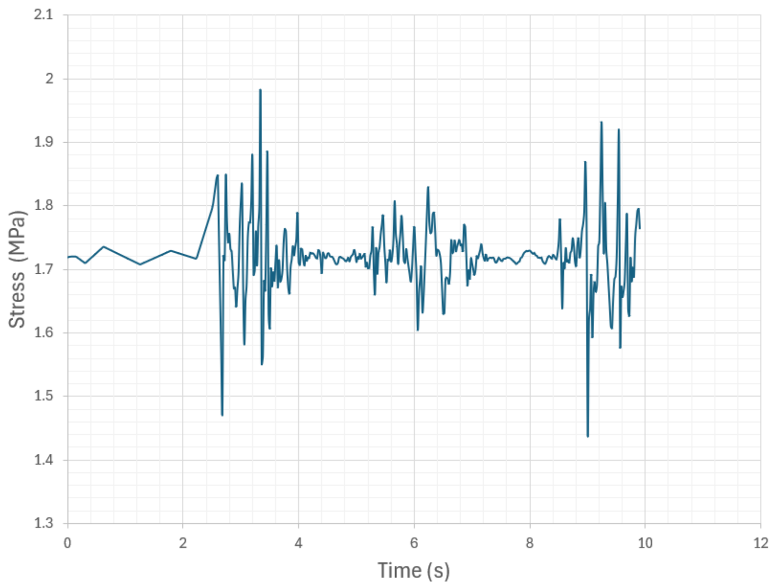

Fig. 3.14. *Max stress in parts made from (solid surface)*

In both cases, the maximum stress is approximately 2 MPa, and, similar to the deformation, it occurs at 3.34 seconds of the simulation. The stress distribution at 3.34 seconds can be observed in Figure 3.15.

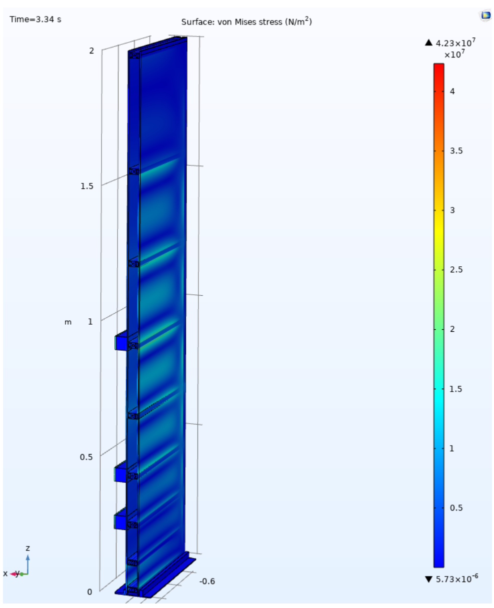

Fig. 3.15. *Max stress at 3.34 s*

3.5. Evaluation of pressure caused by deformations

Pressure caused by deformations is defined as follows in Eurocode 8:

$$p_f(\zeta,\theta,t) = \rho H \psi \cos(\theta) \sum_{n=0}^{\infty} d_n \cos(\nu_n \zeta) A_{fn}(t) \tag{3.6}$$

$$\psi = \frac{\int_0^1 f(\zeta)\left[\frac{\rho_s}{\rho}\frac{s(\zeta)}{H} + \sum_{n=0}^{\infty} b'_n \cos(\nu_n\zeta)\right] d\zeta}{\int_0^1 f(\zeta)\left[\frac{\rho_s}{\rho}\frac{s(\zeta)}{H} f(\zeta) + \sum_{n=0}^{\infty} d_n \cos(\nu_n\zeta)\right] d\zeta} \tag{3.7}$$

$$b'_n = \frac{2(-1)^n I_1\left(\frac{\nu_n}{\gamma}\right)}{\nu_n^2 I'_1\left(\frac{\nu_n}{\gamma}\right)} \tag{3.8}$$

$$d_n = 2\frac{\int_0^1 f(\zeta)\cos(\nu_n\zeta)d\zeta}{\nu_n}\frac{I_1\left(\frac{\nu_n}{\gamma}\right)}{I'_1\left(\frac{\nu_n}{\gamma}\right)} \tag{3.9}$$

where $\phi(\zeta,\theta) = f(\zeta)\cos(\theta)$ is the shape function of the cylindrical wall, ρ_s is the material density of the structure, $s(\zeta)$ is the wall thickness function, and $A_{fn}(t)$ represents the time dependence of acceleration for a simple oscillator with vibration mode n, period, and damping factor. eurocode 8 indicates that it is sufficient to consider $n = 1$. The Absolute oscillator value for construction could be seen on Fig. 3.16.

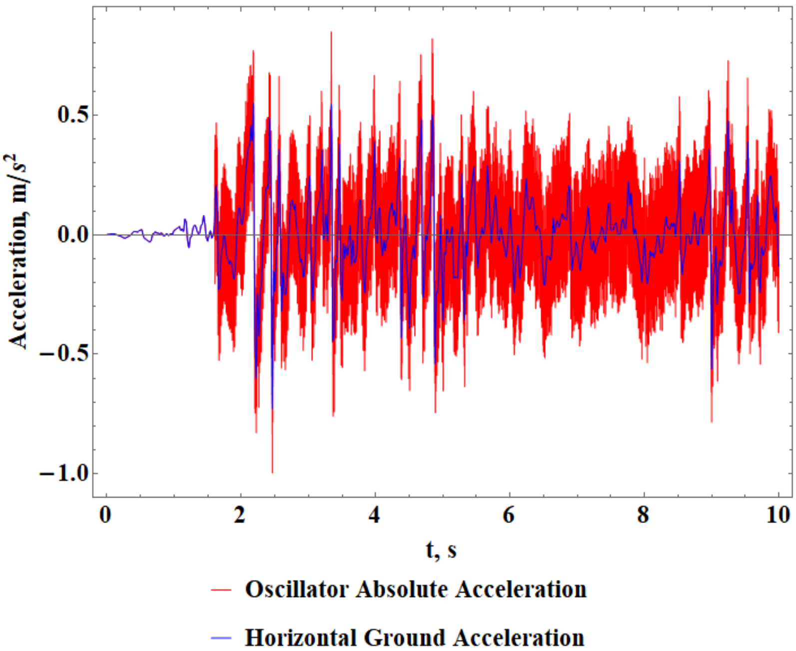

Fig. 3.16. *Absolute oscillator and ground accelirations*

However, the Eurocode utilizes an oscillator relative to the ground, the values of which can be seen in Figure 3.17.

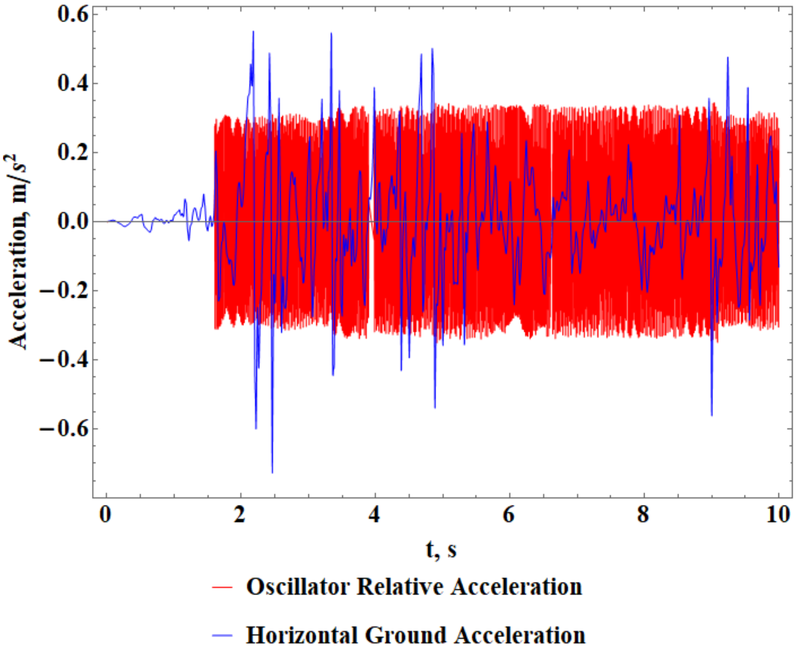

Fig. 3.17. *Relative oscillator to ground and ground accelirations*

It is important to note that the acceleration $A_{fn}(t)$ in both cases is less than one.

For a more conservative assessment of the elastic component of the pressure caused by deformation, it was assumed that the deformation was greater than in reality, reaching 1 mm along the entire length of the vessel. By substituting these values into Equation 3.6, without considering the deformation acceleration factor, the pressure distribution along the vessel wall appears as shown in Figure 3.18.

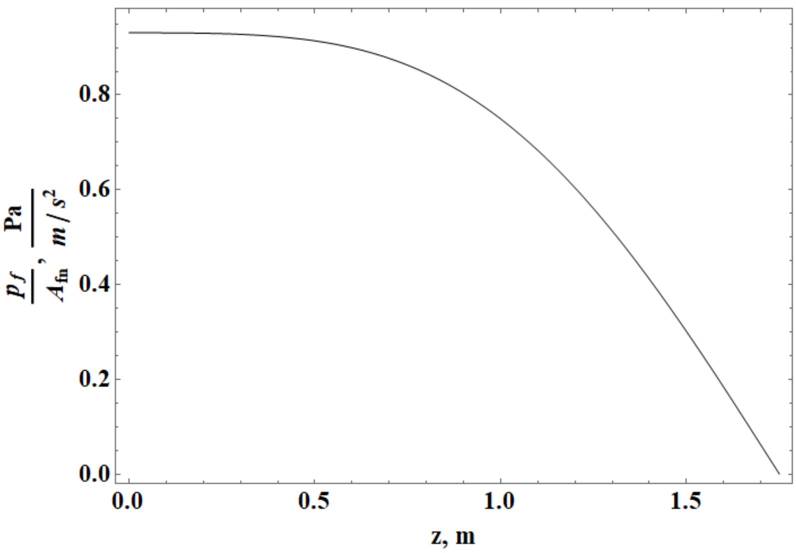

Fig. 3.18. *Relative flexible pressure displacement on wall*

Meanwhile, in reality, the deformation acceleration did not exceed 4 m/s² throughout the entire time period (see Figure 3.19 for reference).

The pressure values, with applying the mode multiplier plus ground acceleration in the worst case, amount to 9 × 4,5 = 40.5 Pa.

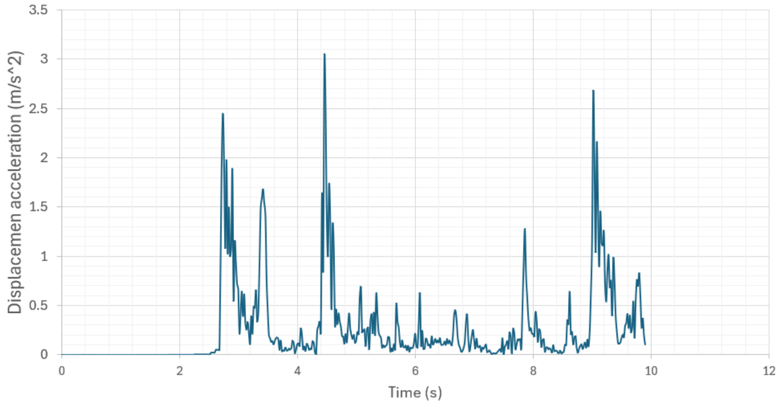

Fig. 3.19. *Displacement acceleration*

From this, it follows that the pressure caused by the deformation of the surface and its interaction with water is insignificant, as it is several orders of magnitude lower than the hydrostatic pressure of the water. This is quite logical, given the low seismic activity and small deformations. Therefore, this component was not considered in the calculations.

3.6. Tanks bottom parts evaluation

The bottom segments of the structure are filled with aluminum honeycomb, which is essentially a non-homogeneous material. Direct calculations for such a geometry can be challenging.

3.6.1. Honeycomb equivalent

The effective homogenized material properties for a honeycomb structure are derived from analyzing the unit cell (repeating element) of the honeycomb. The geometry of the unit cell depends upon the method used to fabricate the honeycomb core. In this report, the honeycomb structure is assumed to be constructed from Data sheet for **AmfiTop** sandwich wall-panel.

The unit cell selected for this study is shown in Figure 3.20. The cell size (d), angle (θ) and thickness (t) completely define any honeycomb geometry of the unit cell. The length of the sides of the hexagonal honeycomb core (L) can be determined from d and θ as shown in Figure 3.20. For a regular hexagonal honeycomb structure, the angle θ equals 30 degrees [12].

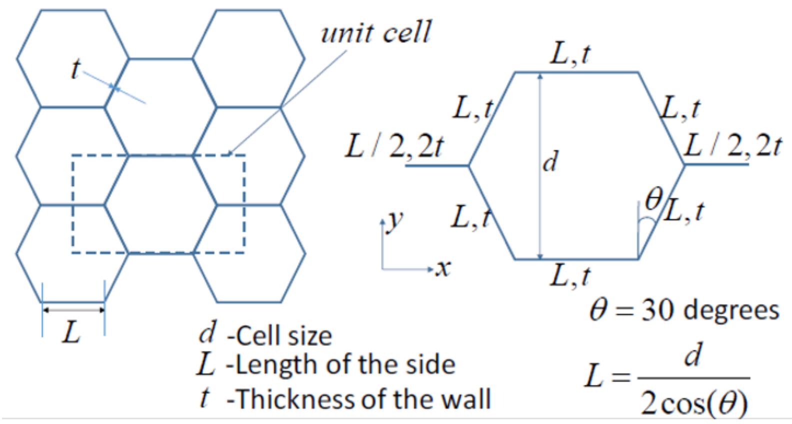

Fig. 3.20. *Unit cell*

The most widely used analytical expressions for the effective material properties of a honeycomb core were derived by Gibson [13]. These analytical expressions were derived assuming the walls of the honeycomb unit cell deform solely due to bending of the inclined walls. The effective in-plane moduli are given by [12]:

$$E_x = \frac{E_c\left(\frac{t}{L}\right)^3\cos(\theta)}{(1+\sin(\theta))\sin^2(\theta)}; \tag{3.10}$$

$$E_y = \frac{E_c\left(\frac{t}{L}\right)^3(1+\sin(\theta))}{\cos^3(\theta)}; \tag{3.11}$$

$$G_{xy} = \frac{E_c\left(\frac{t}{L}\right)^3(1+\sin(\theta))}{3\cos(\theta)}; \tag{3.12}$$

$$\nu_{xy} = \frac{\cos^2(\theta)}{(1+\sin(\theta))\sin(\theta)}; \tag{3.13}$$

where E_c is the elastic modulus of the wall. The out-of-plane elastic properties derived using Gibson's assumptions are presented in Reference [**Reference12**] and are represented by

$$E_z = \frac{\rho}{\rho_c} E_c; \tag{3.14}$$

where $\frac{\rho}{\rho_c}$ is the relative density of the equivalent core and

$$\nu_{xz} = \nu_c \frac{E_x}{E_z}; \tag{3.15}$$

$$\nu_{yz} = \nu_c \frac{E_y}{E_z}; \tag{3.16}$$

$$G_{xz} = G_{yz} = G_c \left(\frac{t}{L}\right) \frac{\cos(\theta)}{1+\sin(\theta)}; \tag{3.17}$$

where ν_c and G_c are the Poisson's ratio and shear modulus of the wall. The Gibson's Equations are valid only for a uniformly isotropic wall material.

The utilized honeycomb core is a regular hexagon core with the geometric properties and density listed in Table 3.4.

Table 3.4. *Geometric properties and density of utilized honeycomb core*

Material	**Wall length** (L, mm)	**Wall thickness** (t, mm)	**Density** (ρ_{core}, kg/m^3)
Aluminium alloy	3.72	0.06	75

The nine equivalent elastic parameters of honeycomb core given in Table 3.5 are estimated based upon formulas starting from Gibsons equation.

Table 3.5. *Equivalent material properties of the honeycomb core*

Elastic properties		**Unit**
E_x	0.68	[MPa]
E_y	0.68	[MPa]
E_z	1944	[MPa]
G_{xy}	0.17	[MPa]
G_{xz}	245.1	[MPa]
G_{yz}	245.1	[MPa]
ν_{xy}	1.0	–
$\nu_{xz} = \nu_{yz}$	0	–

3.6.2. Bottom element calculation results

To evaluate the bottom segment, symmetry was used, similar to the approach taken for the wall. The selected segment and applied symmetry conditions can be seen in Figure 3.9.

Based on previous calculations, it was determined that the maximum pressure occurs at 3.34 seconds of the simulation. Therefore, for the strength analysis of the bottom, the pressure from this time interval was applied in a static analysis. The results of the numerical model can be observed in Figure 3.21.

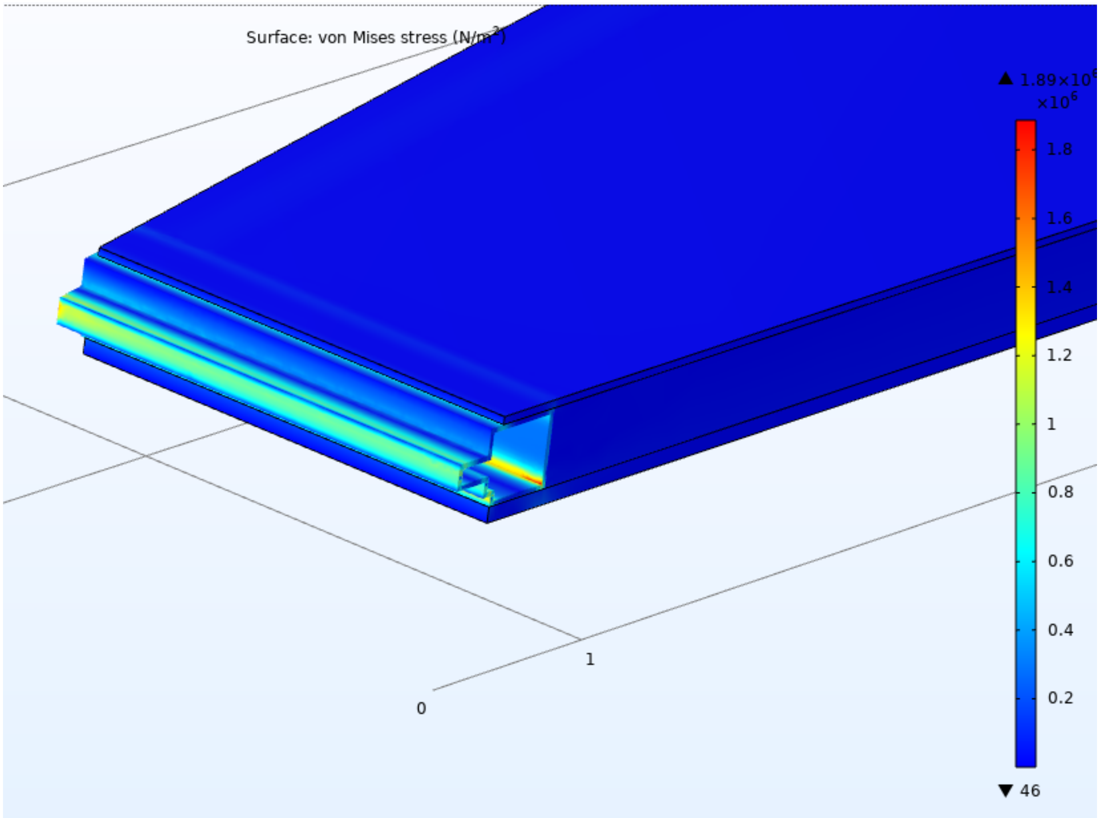

Fig. 3.21. *Stress in bottom element*

The maximum stress in the structure was 1.89 MPa. A detailed analysis indicates that:

- The maximum stress in the aluminum profiles did not exceed 1.89 MPa.
- The maximum stress in the Solid Surface components was 0.8 MPa.
- The stress in the honeycomb core did not exceed 0.48 MPa under compression.

Thus, it can be concluded that this structural element withstands the applied load and has a high safety factor.

4. Mesh and geometry optimization

4.1. Geometry optimization for qualitative mesh

It is important to note that the proper construction of the mesh is a crucial component of accurate calculations. If the dimensions are incorrect or the shape of the elements is inadequate, it is easy to obtain inaccurate results, or the calculation may not converge at all.

To create a high-quality mesh, artifacts in the geometry were eliminated, as they most likely arose due to rounding errors during the design stage. An example of such an artifact can be seen in image 4.1.

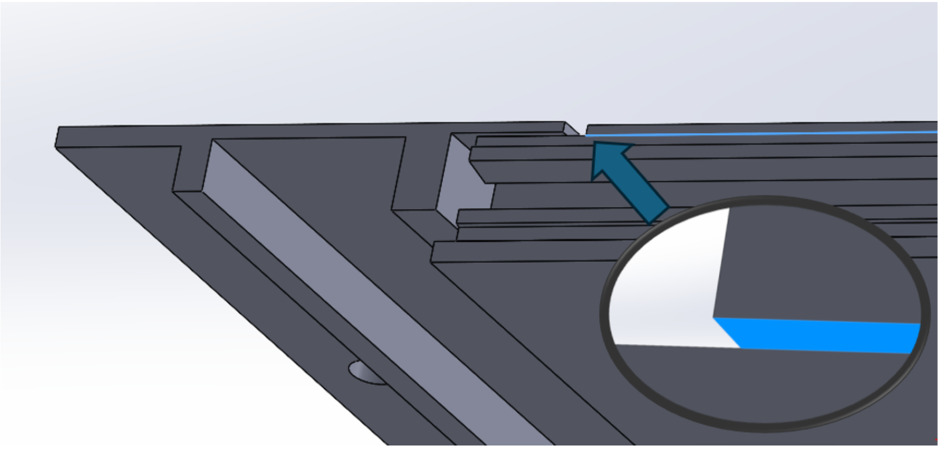

Fig. 4.1. *Enter Caption*

In image 4.1, it is visible that two parts are not in the same plane, resulting in a small edge less than a 0.01 millimeter wide. While this does not cause issues in manufacturing, such edges can create elements of very low quality when generating the mesh, see fig 4.2 where low quality of mesh elements is represented with red light.

Therefore, during the modeling process, numerous inaccuracies were corrected to achieve more precise results.

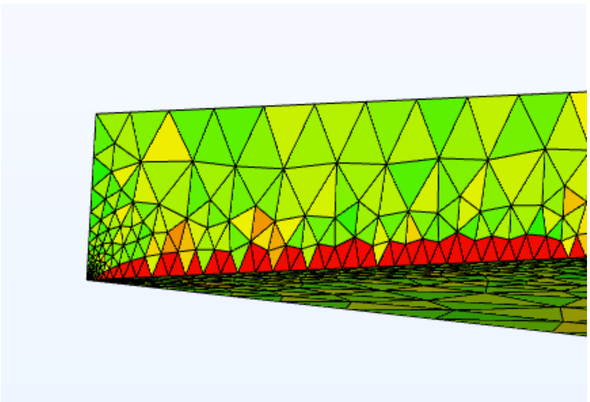

Fig. 4.2. *Low quality element example*

4.2. Mesh quality evaluation

As previously stated, the mesh can significantly impact the accuracy of calculations. Therefore, for many structural components, it was generated separately, see example of mesh 4.3.

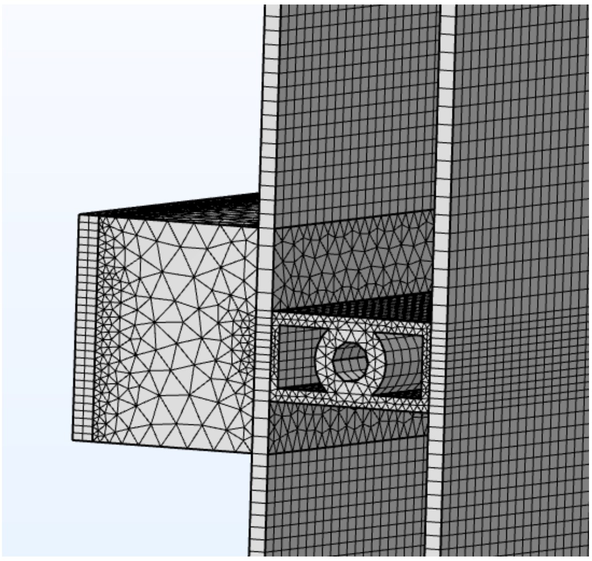

Fig. 4.3. *Generated mesh example*

Unfortunately, neither visual inspection nor automated quality analysis alone can determine whether a particular mesh is suitable for the given model.

Consequently, multiple mesh variations with different element counts were created, and their results were compared using hydrostatic loading in a static analysis. A comparison of these results can be seen in Figure 4.4.

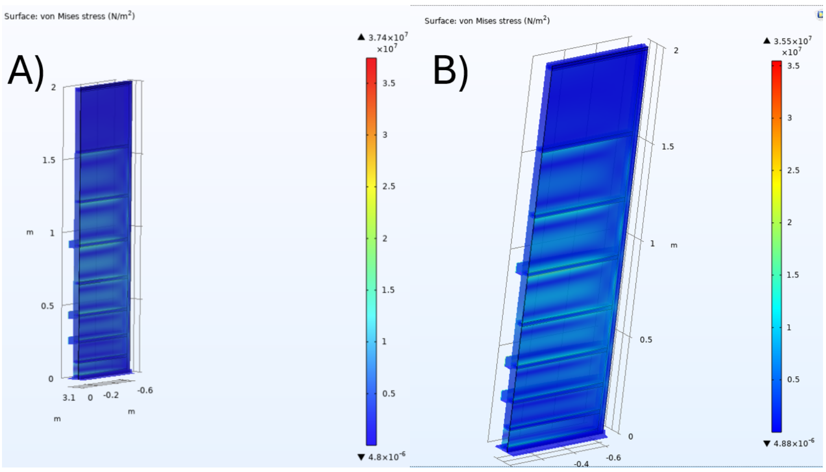

Fig. 4.4. *Results with defferent mesh resolution mesh A) Is 860k elements and B) is 1157k elements*

Figure 4.4 presents the results of a simulation using different mesh element counts: 860k and 1157k elements. First of all, in both cases can't be seen any unrealistic stress location, the values are smooth. Despite the element count differing by more than 34%, the maximum stress varies by less than 5%, indicating a good approximation of the geometry with the mesh.

4.3. Geometry optimization

The initial geometry of the pool structure included steel tension belts located on the surface of the wall. In fig. 4.5, they are marked in red.

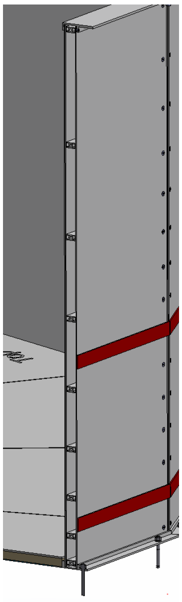

Fig. 4.5. *Initial construction design*

However, calculations, an example of which was presented above, indicated that the initial belt engineering solution does not resolve the issue of the critical moment arising in the structure, even under hydrostatic load. Therefore, spacers made of 'Solid Surface' material were added to the design, the number of belts was increased to three, and their placement was also modified. The spacers, as seen on a segment of the wall are marked with blue color, can be observed in fig. 4.6.

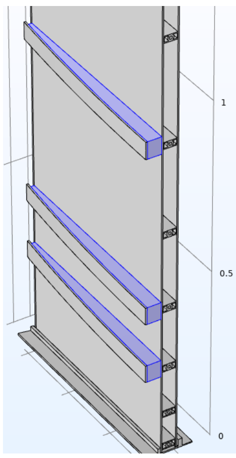

Fig. 4.6. *Spacer allocation*

5. Conclusions

A literature review and initial calculations indicate that this task allow the use of simplified methods.

Was numerically proven that a cylindrical structure described in European standards can adequately approximate the tested geometry.

The numerical analysis demonstrated that the structure with diameter of 6 m and 1.75 m water hight is capable of withstanding both hydrostatic loads and dynamic loads caused by seismic activity, as described in the data provided by the client. Important to note that behavior factor were used as 1 at the same time for tanks according to Eurocode 8 could be used 1.5 which means that construction is even more safe. It is important to note that in this case, the dominant load is hydrostatic pressure, as seismic activity is relatively low.

Additionally, the influence of pressure caused by structural deformation was numerically evaluated. The results indicate that, due to a combination of factors such as the geometry of the structure and the nature of the seismic load, this pressure is insignificantly small.

For more accurate calculations and the absence of plastic deformations, the geometry was optimized.

Bibliography

[1] *Eurocode 8: Design provisions for earthquake resistance of structures : General rules, specific rules for various materials and element.* London: BSI, 1996, Merged with DD-ENV-1998-1-1 and DD-ENV-1998-1-2 into prEN-1998-1.

[2] M. Porcu, *A short note on the different methods of seismic analysis*, vol. 1, 2020.

[3] M. Porcu and L. Chessa, *How code-based linear static analysis for seismic design of masonry buildings may fail to be conservative*, Ingegneria Sismica, vol. 4, pp. 13–28, 2011.

[4] A. Paglietti, M. Porcu, and M. Pittaluga, *A loophole in the eurocode 8 allowing for non-conservative seismic design*, Engineering Structures, vol. 33, no. 3, pp. 780–785, 2011.

[5] H. Altun and A. Gedikli, *Seismic analysis of steel liquid storage tanks by api-650*, 2013.

[6] A. Rashed, G. Mahmoud, N. Eid, and A. Talaat, *3d analysis for conical tanks under seismic loads*, vol. 16, pp. 29–44, 2019.

[7] A. Eraky, k. essam khaled, and A. Salama, *Evaluation of the methodology for seismic analysis of elevated water tanks using different international codes of practice*, 2024.

[8] M. Sivy and M. Musil, *Seismic resistance of storage tanks containing liquid in accordance with principles of eurocode 8 standard*, Journal of Mechanical Engineering, vol. 66, 2016.

[9] A. Tsouvalas, T. Molenkamp, K. Canny, D. Kroon, M. Versluis, Y. Peng, and A. Metrikine, *A mode matching technique for the seismic response of liquid storage tanks including soil-structure interaction*, 2020.

[10] M. Musil and M. Sivy, *Seismic response of elevated liquid storage tanks*, in *Aplimat Conference*, 2017.

[11] F. Ferreira, C. Moutinho, A. Cunha, and E. Caetano, *An artificial accelerogram generator code written in matlab*, Engineering Reports, vol. 2, 2020.

[12] A. Korjakins, *Preliminary work: Finite element model of fish tank*, RTU, Tech. Rep., version REV.2, 2024.

[13] L. J. Gibson, M. F. Ashby, G. S. Schajer, and C. I. Robertson, *The mechanics of two-dimensional cellular materials*, Proceedings of the Royal Society A: Mathematical, Physical and Engineering Sciences, vol. 382, no. 1782, pp. 25–42, 1982.

Appendix 1 to the Contract

WORKPLAN

for earthquake stability calculation of basin for aquaculture in accordance with rules of Eurocode 8

1. Advanced Literature Analysis on Structural Engineering Approaches: Simplified Design vs. Eurocode and Scaling to Detailed Larger Structures
2. Geometry Creation Taken in Account Dynamic Interaction Between Solid and Liquid Phases.
3. Simplification of Geometry and Composite Material Properties.
4. Simplification of Panel Connections.
5. Mesh Generation with Necessary Refinement in Critical Zones.
6. Evaluation and Optimization of Model and Calculation Method.
7. Stability Calculation for Basin with Given Geometrical and Physical Data.
8. Final Report with Description of Models, Methods and Results.

____________________ ____________________

S. Fürstenberg G. Kitenbergs

Report maximum seismic load for Norway

March 2024

NORSAR

Executive summary

Probabilistic seismic hazard studies are estimating the maximum ground shaking intensity at given probability levels or return periods. Such hazard estimates may be used as basis for design or in risk analyses for the purpose of protecting life, health, environment, and investments.

The present investigations and analyses with resulting seismic loading for Norway have been conducted between 2018 and 2020 with the aim of substituting the 20-year-old results documented by NORSAR and NGI (1998). The study is based on an updated earthquake catalogue and on an improved Probabilistic Seismic Hazard Analysis (PSHA) methodology.

Improved earthquake event observations and enhanced earthquake catalogue

A complete review and revision of the existing historical earthquake catalogue was conducted, from the first historical reports to the latest small magnitude instrumental locations. Many erroneous reports were removed or corrected, mainly through detailed analysis, but also through global parametrized processing. For example, small on-shore day-time events suspected to be man-made explosions were removed. This process leads to a homogenized earthquake catalogue, covering both onshore and offshore earthquake activity. The enhanced earthquake event database was the basis for the quantification of the seismicity, starting with computation and determination of seismic hazard parameters: completeness (time-magnitude) and earthquake size distribution.

New development and improvement in the PSHA related methodologies and tools

The development of the new seismic zonation map has involved the implementation of several methodologies and analysis steps that have been improved significantly since 1998. Available software solutions have also improved significantly, leading to more sophisticated modelling of earthquake events. The resulted new seismic zonation was obtained for a specific reference horizon adequate for the concept of a well-defined shear-wave velocity profile (Vs30, time- averaged shear-wave velocity to 30 m depth), a concept that was not incorporated in 1998.

Because of the relatively low and disperse seismic activity in most of the regions of Norway, a number of larger mega-zones were defined from southern Norway to northern Spitsbergen, and for each of these zones the completeness and earthquake size distribution were established using a variety of statistical methods.

A vital part of the investigation was put into a review of the known geology (geological structures and mapped faults) and the historical and contemporary seismicity was merged into a regional seismotectonic concept. This concept is implicit in the definition of zones and mega-zones, and it expresses the various expert judgements and the quantification of the final computational model. The final combined hazard has been modelled with the aim to capture the inherent epistemic uncertainty of future earthquake locations.

Using the zonation free method, which was not possible in 1998, the geographical distribution of the seismicity and the earthquake recurrence within each zone are mapped in a grid, where the seismic activity rates, the earthquake size distribution scaling and the maximum magnitude are individually computed for each geographical grid point.

Since 1998, significant developments in spectral attenuation (Ground Motion Prediction Equations–GMPE) have taken place. As of 2018, about 750 different GMPEs have been developed from the observation of earthquake shaking intensities as function of magnitude, distance, and frequency. Due to the important influence on the hazard results that the GMPE relations exert, four different relations, identified as the most appropriate and representative of the tectonic environment for Norway, have been used to do the computations in a logic tree setup. In doing so, the significant epistemic uncertainties in such prediction models are taken into account. In addition, a vital piece of information on subsurface shear wave velocities in Norway was brought forward by the Norwegian Geological Survey (NGU) obtained from more recent crustal drilling. Analysis of the data from these drillholes recommended and justified the use of 1200 m/s as the reference shear wave velocity for Norwegian competent rock sites.

The final hazard results are provided as equal hazard response spectra in terms of spectral acceleration for rock sites (Vs = 1200 m/s) for 5 % damping corresponding to 10 % in a 50-year exceedance probability.

A note regarding application

The results provided through the present investigations and analyses have been obtained using a reference shear wave velocity of 1200 m/s. This is in line with the assumption made in EC8, where the shear wave velocity for rock sites is defined as Vs>800 m/s. The report is directly providing ground acceleration a_{gR}.

Disclaimer

This report represents an executive summary of the comprehensive work that has been undertaken in the recent years to produce the new seismic zonation map for Norway and Svalbard, as verified by international experts within the relevant fields.

NORSAR's services and products concerning seismic hazards have been developed within a probabilistic framework. NORSAR may not be held liable for any claims, damages or losses which in any way is connected to reliance upon NORSAR's services or products concerning seismic hazards of any sort, including but not limited to earthquakes, landslides, avalanches or movement in rock massifs housing or supporting infrastructure and possible consequences of such events. The limitation also applies to any claims, damages or losses any party might have as a result of reduced activity, interest in, or value of assets affected by NORSAR's indications and/or estimates of seismic hazards, regardless of whether the indications/estimates are accurate or not.

Seismic load is generated from the seismic zonation map for Norway and Svalbard v.1.0.2019

Load estimates for Eurocode 8 applications

Date:	2024-03-06
User:	Ivan Van Bever
Seismic ground acceleration generated for:	Berg, v_s = 1200 m/s
Project name:	Maximum seismic load for Norway / Svein Fürstenberg

Input

Return period:	475 years
Ground type:	A

NORSAR
Postadresse:
Postboks 53
2027 Kjeller

Besøksadresse:
Gunnar Randers vei 15
2007 Kjeller

info@norsar.no
www.norsar.no

Foretaksregisteret:
Org.nr: 974 374 765 MVA
Bank: DNB Lillestrøm
SWIFT: DNBANOKK

Konto nr: 7102.05.03283
IBAN (NOK): NO78 7102 0503 283
IBAN (EUR): NO47 5019 0447 100
IBAN (USD): NO95 7004 0444 562

Result for return period 475 years

1. Uniform Hazard Response Spectrum

Maximum reference peak ground acceleration on type A ground (from the seismic zonation map for Norway excluding Svalbard) a_{gR}: **0.5832 m/s²**

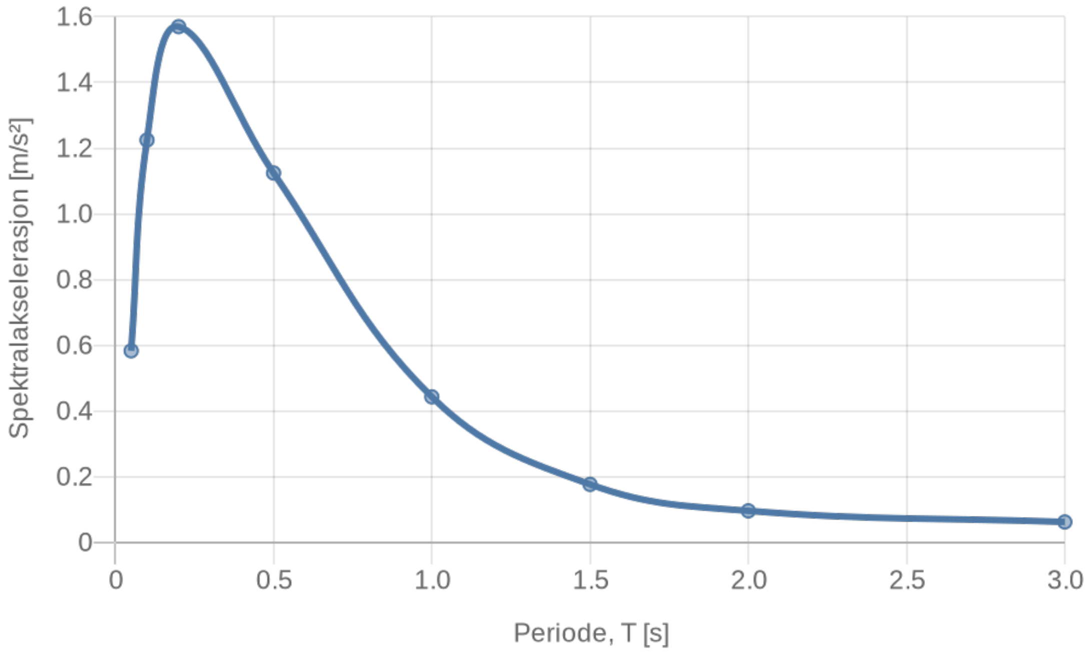

2. Horizontal elastic response spectrum

Parameters describing the horizontal elastic response spectrum

Ground type	S	T_B	T_C	T_D
A	1	0.05	0.25	1.2

3. Vertical elastic response spectrum

Parameters describing the horizontal elastic response spectrum

Ground type	T_B	T_C	T_D
A	0.05	0.15	1.00

NORSAR
Postadresse:
Postboks 53
2027 Kjeller

Besøksadresse:
Gunnar Randers vei 15
2007 Kjeller

info@norsar.no
www.norsar.no

Foretaksregisteret:
Org.nr: 974 374 765 MVA
Bank: DNB Lillestrøm
SWIFT: DNBANOKK

Konto nr: 7102.05.03283
IBAN (NOK): NO78 7102 0503 283
IBAN (EUR): NO47 5019 0447 100
IBAN (USD): NO95 7004 0444 562

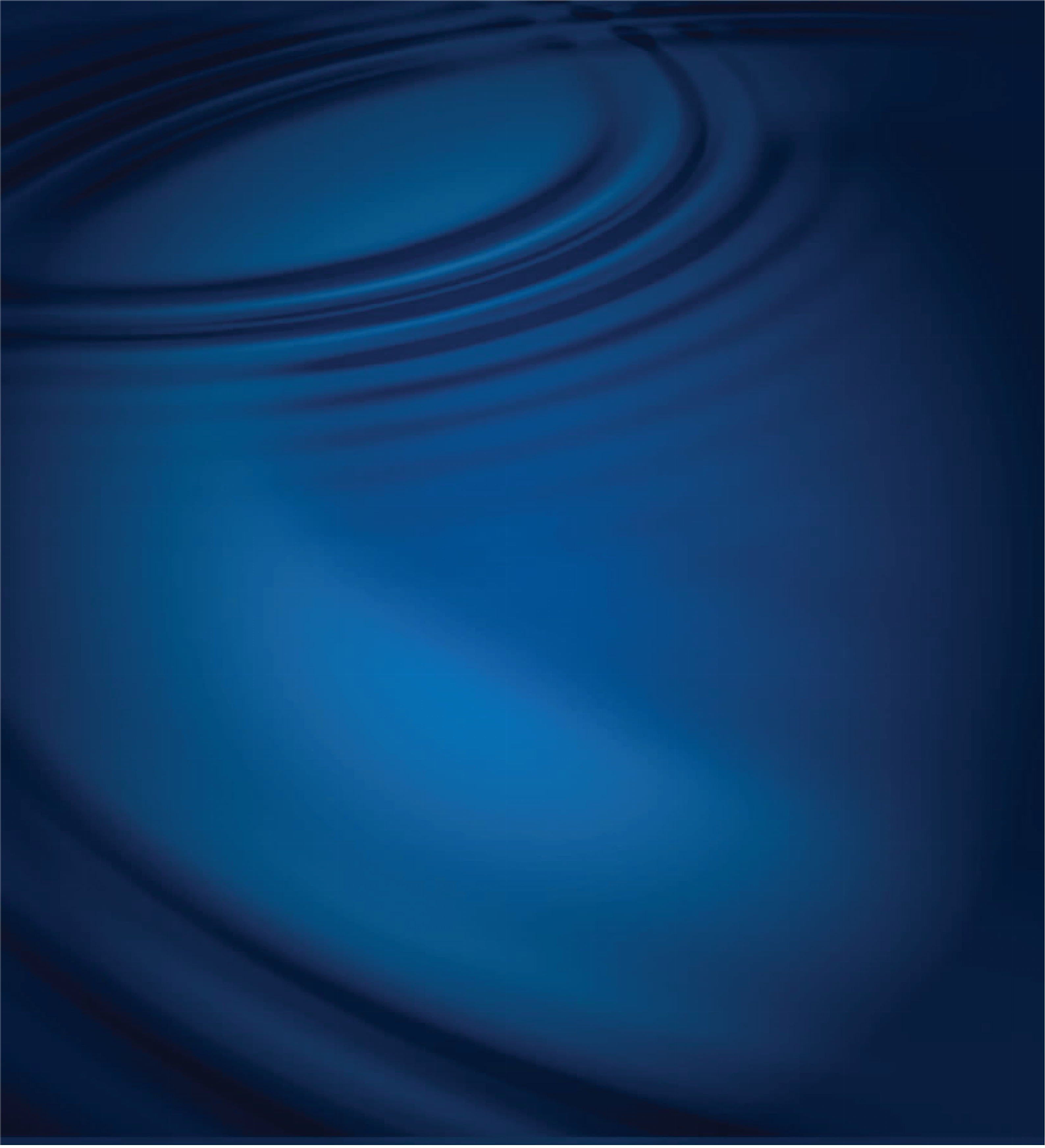

info@norsar.no
www.norsar.no